Journal of Systems Engineering and Electronics
Vol. PP, No. 99, November 2023, pp.1 – 17

Contact detumbling toward a nutating target through deformable effectors and prescribed performance controller

ZANG Yue[1], ZHANG Yao[1,*], HU Quan[1], LI Mou[2], and CHEN Yujun[2]

1. School of Aerospace Engineering, Beijing Institute of Technology, Beijing 100081, China;
2. China Academy of Space Technology, Beijing 100029, China

Abstract: Detumbling operation toward a rotating target with nutation is meaningful for debris removal but challenging. In this study, a deformable end-effector is first designed based on the requirements for contacting the nutating target. A dual-arm robotic system installed with the deformable end-effectors is modeled and the movement of the end-tips is analyzed. The complex operation of the contact toward a nutating target places strict requirements on control accuracy and controller robustness. Thus, an improvement of the tracking error transformation is proposed and an adaptive sliding mode controller with prescribed performance is designed to guarantee the fast and precise motion of the effector during the contact detumbling. Finally, by employing the proposed effector and the controller, numerical simulations are carried out to verify the effectiveness and efficiency of the contact detumbling toward a nutating target.

Keywords: nutating target, contact detumbling, dual-arm space robot, deformable end-effector, prescribed performance controller.

DOI: 10.23919/JSEE.2023.000121

1. Introduction

Operations dealing with space debris are of great concern [1-3] since space debris is increasing year after year. For fast-rotating targets, the detumbling process of the target is an effective means to reduce the risks of on-orbit capture and removal. Thus, a variety of contactless [4,5] and contact detumbling [6,7] technologies have been studied. Contact detumbling through robotic arms has a stronger contact effect and better controllability than the contactless methods, which makes it an attractive research area.

In a previous study [8], an ideal contact detumbling situation toward a sphere rotating target was proposed to demonstrate the feasibility of continuous contact detumbling and the effectiveness of restricting the displacement of the target. However, space debris like failed satellites is commonly not a sphere target but has an irregular structure with attachments, such as solar panels. In addition, inspired by the complex disturbance in space, the target motion may exhibit nutation rather than rotation along one axis. These factors make the already complex detumbling operation more challenging.

To detumble a target considering its nutation motion, Liu et al. [9] modeled a detumbling system that consists of a service satellite and a cubic rotating target. They proposed a discontinuous contact method using a soft rod and verified the high efficiency of detumbling through numerical simulations. Wang et al. [10] used a spring rod contactor to touch the edge of the solar panel when the target is rotating with nutation. Then, numerical simulations verified that the developed optimal contact control method is effective for detumbling and has certain robustness to measurement and identification errors. However, some problems, such as the selection of the touching area and tackling the displacement of the target, are not considered in the above studies. In addition, rod actuators have difficulty balancing contact detumbling and thereafter capture operations. Wu et al. [11] used an undeformable gripper to contact and capture a slow-tumbling object. The gripper was modeled as an arm link with a specific structure, and its operation capacity was not outstanding. However, for contact detumbling toward a target rotating with nutation, the detumbling operation needs to have higher accuracy, greater operational dexterity, and faster motion response to make the contact steady and effective. As the actuator of contact detumbling, the end-effectors are expected to be more dexterous to cooperate with the robotic arms for accurate contact operation.

Compared with the above actuators, deformable actuators increase the dexterity of the robotic system and are capable of accurate operations such as industrial manu-

Manuscript received January 04, 2022.
*Corresponding author.
This work was supported by the National Natural Science Foundation of China (11972077; 11672035)

facturing [12] and aerospace research [13]. Some actuators deform through the material characteristics and are more suitable for grabbing objects with different shapes, such as multiple articulated grippers [14] and ionic polymer-metal composite actuators [15]. Some actuators deform through the mechanical drive and have greater structural stiffness. Han et al. [13] designed and tested a deformable claw for on-orbit docking of space mechanisms, and the actuator operates powerfully and satisfies the working requirements. Feng et al. [16] proposed a similar three-claw end-effector for self-relocation and payload handling, and its kinetic characteristics are described in detail. For the contact detumbling toward a target rotating with nutation, a large deformation range of the actuator is needed to suit the movement of the contact surfaces, a great structural strength is also needed to maintain the contact strength. Thus, it is meaningful to design a distinctive deformable end-effector for detumbling a target rotating with nutation.

Since the complex motion and shape of the target cause the contact point jumping, the end-effector is required to move and deform quickly to achieve safe and effective contact detumbling. The motion performance of the end-effector depends not only on the structure of the end-effector but also on the characteristics of the controller. The robot joints are considered capable of actuating the controller ideally due to the advanced joint torque measurement and motor technology [17]. Complex and powerful controllers are designed for the robotic arm to perform more precise and complex on-orbit operations. In existing studies, Wang et al. [10] designed an optimal contact controller to eliminate the rotation and damp the nutation for the spinning target object, and the control method gains robustness to the measurement and identification errors of the target object during the operation. Ge et al. [18] controlled a dual-arm robot using an impedance control method for contacting and capturing a tumbling target, through which the contact forces can be constrained to remain safe. In [19], a dual-arm robot was used to detumble and capture a cylinder spinning target, and the desired arm motion and contact detumbling are realized by a hybrid control method combining computed torque control and sliding mode control. Liu et al. [20] used a position-based overdamping control method to keep the contact continuously during detumbling. Zong et al. [21] proposed a shortest-time detumbling trajectory and generated the desired motion through a coordinated controller designed by substituting both the motion of the robot body and the arm joints.

To achieve a satisfying contact detumbling upon a rotating target with nutation, the controller is expected to have a clear, preferably quantitative performance to guarantee the contact effect. Prescribed performance controller (PPC) [22] features in directly designing the performances of the tracking error such as the error boundary and convergence rate. Therefore, PPC can strongly constrain the system even if the system meets with uncertainties and disturbances such as the non-cooperative spacecraft proximity [23] and safety flight of the unmanned aerial vehicle [24]. Aiming to obtain great tracking motion performance for a robotic system, Liu et al. [25] combined PPC with the dynamic surface control method for achieving an accurate trajectory tracking of a free-flying flexible-joint space robot. Zheng et al. [26] combined PPC with the super-twisting adaptive sliding mode control and overcame the unknown disturbances and structural uncertainties of the surgical robot manipulator, the controlled system shows high operation precision and strong anti-disturbance ability. Dealing with the problem of the unknown inertial properties and external disturbance of a space robot-target combination, Wei et al. [27] proposed a learning-based adaptive PPC and obtained great performance on attitude takeover.

To satisfy both detumbling efficiency and operation safety under the contact disturbance and tracking error of the operation, the controller of the robotic system needs to have not only the ability to directly design the performances but also to adapt to the system parameters. Therefore, an adaptive sliding mode controller with prescribed performance is employed for detumbling a rotating target with nutation. However, PPC with traditional error boundaries is extremely strict about the tracking error and has a high demand for control bandwidth. In addition, the continuous disturbances of the contact require the controller to be more robust for stable control outputs. Thus, a new tracking error boundary is designed to improve the robustness of the controller, and a prescribed performance adaptive sliding mode controller (PPASMC) that adapts to the robotic system in this paper is designed for successfully and satisfactorily detumbling a rotating target with nutation.

In summary, this paper studies the features and performance of the contact detumbling toward a cubic target rotating with nutation that by employing a deformable end-effector and a high-performance controller. First, the end-effector is designed with a large deformation range to suit the different contact areas and the motion requirements during the contact calculated from the target motion. The end-effectors are modeled together with the arms to better adapt to operation planning and control in the following sections. Then, to overcome the uncertainty and variation of the contact, a PPASMC is designed to manage the whole robotic system for dissi-

pating the target motion. Finally, according to the numerical simulations, the effectiveness and efficiency of the contact detumbling through the proposed deformable end-effector and the controller are verified and analyzed.

The organization of this paper is as follows: Section 2 designs a deformable end-effector that can adapt to the contact operation based on the analysis of the motion characteristics of the target. Then, the complete robotic system with the deformable end-effectors is modeled. In addition, the deformation characteristics of the deformable end-effectors are illustrated through a motion comparison with the undeformable end-effectors. Section 3 gives the control loop of the robotic system and the controller requirements. Then, the PPASMC is designed and its stability is proved. Then in Section 4, numerical simulations of the contact detumbling are given employing the designed end-effector and the controller and are analyzed. Conclusions are drawn in Section 5.

2. Design and model of a hand-shaped deformable end-effector

In this section, the requirements of the end-effectors for safe and effective contact are obtained from the analysis of the target motion, which directs the design of the deformable end-effectors. Then, a dynamic model of the robotic system installed with deformable end-effectors is built, based on which the motion adjustment characteristics are simulated.

2.1 Contact method toward a nutating target and the functional requirements of the effectors

A cubic target rotating with nutation is waiting to get detumbled in this paper. Similar to [8], a dual-arm robot is employed to contact the target, as shown in Fig. 1. To detumble the target safely and effectively, the requirements of the end-effectors for detumbling are analyzed first.

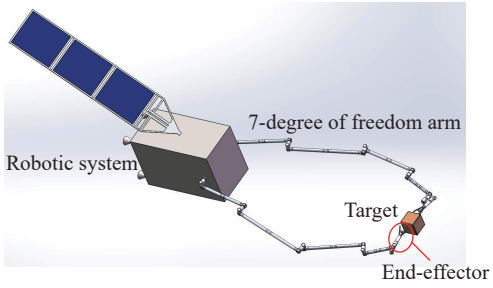

Fig. 1 Contact detumbling scene

The suitable touching surface of the target is determined by both the motion and the structure of the target. When the cubic target rotates along one axis, the two surface perpendicular to the rotating axis is steady in both position and direction, so these areas are suitable to touch. But the nutation of the target reduces the motion stability of the prospective contact area. For example, a cubic target rotates at [1, 20, −1] °/s, its motion envelope is larger than the target itself, as shown in Fig. 2.

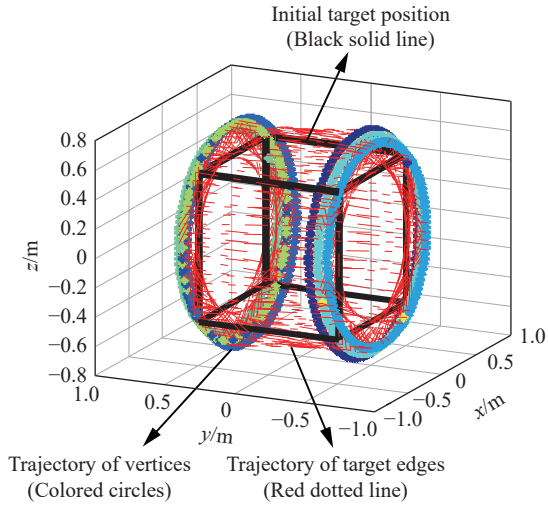

(a) 3D motion envelope of the target

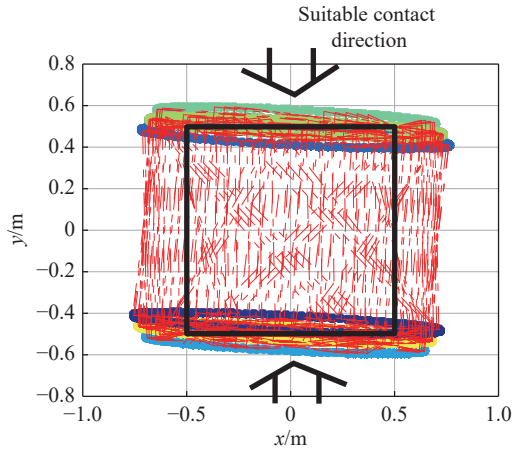

(b) Motion envelope of the target in *X*-*Y* plane

Fig. 2 Motion envelope of the rotating targe

The direction of the prospective contact surface ranges within 10°. The jumping height of points on the prospective contact surface along the main rotating axis ranges from 2 cm to 8 cm. The greater the jumping height of the contact point, the more dangerous and challenging it is to implement the contact operation. To ensure contact safety, the target whose nutation component accounts for no more than 5% of the rotation is able to contact detumbling through the method of this paper.

Considering the rotation of the target, the end tips of the effectors generate circle trajectories on the touching surface, as shown in Fig. 3.

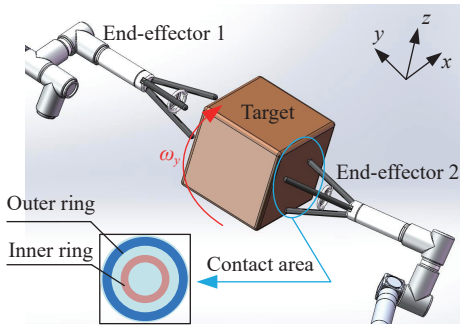

Fig. 3 Ideal contact configuration

When contacting the inner ring, the contact point jump caused by nutation is small, so the collision is gentle, but the detumbling torque generated is also small since the lever arm is relatively short. In contrast, the collision strengthens, and the contact is unstable when contacting the outer ring, but the detumbling torque is enlarged. Thus, the contact position needs a balance between the collision risk and the detumbling efficiency, and the position may adjust during the contact to adapt to different requirements.

In addition to the adjustment of the contact position, in order to further alleviate the relative motion between the tips of the effector and the contact area of the target, the end-effectors are expected to follow the nutation rotation of the target at the same frequency. It is assumed that the motion state of the target has been known through observation and other means and the details of the target observation will not be described in detail in this paper.

The above contact method toward a nutating target requires that the end-effector can deform to adjust the contact position and the joint linking to the effector can rotate nimbly and accurately. Consequently, a hand-shaped deformable end-effector is designed in this paper. And the joint linking to the effector is designed to have multi degrees of freedom.

2.2 Design of a hand-shaped deformable end-effector

Referring to the synchronous motion mode of the parallel drive mechanism, a hand-shaped deformable end-effector with a simple structure and driving method is proposed.

As shown in Fig. 4(a), the deformable end-effector consists of a palm, three fingers, and a drive mechanism. The drive mechanism, enlarged in Fig. 4(b), drives the manipulator to deform through a ball screw. The wheel and connectors translate the linear motion of the drive mechanism to the synchronous opening and closing of the fingers. Each cylinder finger has a dovetail groove to suit the connector. Three fingers are evenly distributed around a palm and are linked by column hinges. When the driving mechanism moves toward the palm, the finger opens, and when it moves backward, the finger closes.

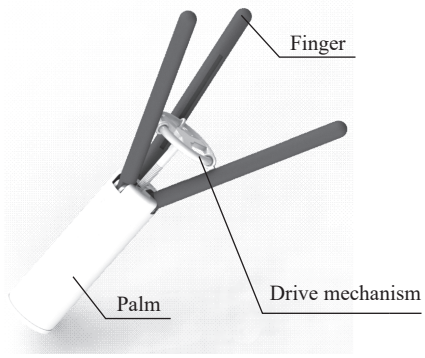

(a) Structure of the end-effector

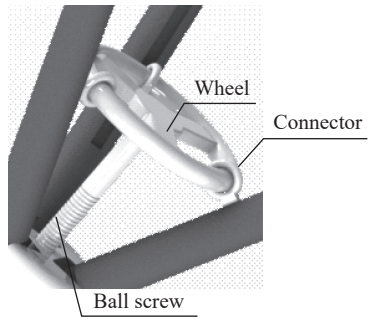

(b) Enlarged structure of the drive mechanism

Fig. 4 Structure of the hand-shaped deformable end-effector

As shown in Fig. 5, f_h^i represents the coordinate system of the end-effector installed on the ith arm. The coordinate system is fixed to the effector, and its x-axis points from the palm to the center of the driving wheel. The coordinate system of the pth finger $f_{\text{fin}\_p}^i$ has the same origin as f_h^i. $f_{\text{fin}\_p}^i$ is fixed to the finger, its x-axis coincides with the finger and points to the end tip.

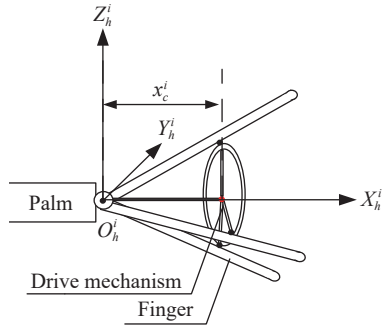

(a) Kinematic diagram of the end-effector

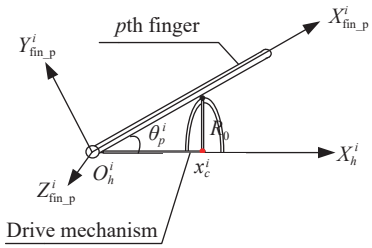

(b) Kinematic diagram of one finger

Fig. 5 Structure diagram of the end-effector

The drive mechanism moves along the X^i_h only, and its scalar position is defined as x^i_c. Written as a vector in f^i_h, the drive mechanism position is

$$\boldsymbol{x}_c^{if^i_h} = \begin{bmatrix} x^i_c & 0 & 0 \end{bmatrix}^{\mathrm{T}}. \tag{1}$$

Correspondingly, the velocity and acceleration of the drive mechanism are

$$\begin{cases} \dot{\boldsymbol{x}}_c^{if^i_h} = \begin{bmatrix} \dot{x}^i_c & 0 & 0 \end{bmatrix}^{\mathrm{T}} \\ \ddot{\boldsymbol{x}}_c^{if^i_h} = \begin{bmatrix} \ddot{x}^i_c & 0 & 0 \end{bmatrix}^{\mathrm{T}} \end{cases} \tag{2}$$

where $\dot{x}^i_c$ and $\ddot{x}^i_c$ are the scalar values of the velocity and acceleration along the X^i_h.

As shown in Fig. 5(b), the radius of the wheel is defined as R_0. The angle between the pth finger and X^i_h is defined as the opening angle θ^i_p. The finger rotates around $Z^i_{\text{fin}\_p}$, so the vector of the opening angle written in $f^i_{\text{fin}\_p}$ is

$$\boldsymbol{\theta}_p^{if^i_{\text{fin}\_p}} = \begin{bmatrix} 0 & 0 & \theta^i_p \end{bmatrix}^{\mathrm{T}}. \tag{3}$$

The rotation of the pth finger can be represented by the movement of the drive mechanism

$$\begin{cases} \boldsymbol{\theta}_p^{if'_{m-p}} = \begin{bmatrix} 0 & 0 & \arctan\left(\dfrac{R_0}{x^i_c}\right) \end{bmatrix}^{\mathrm{T}} \\ \boldsymbol{\omega}_p^{if'_{m-p}} = \begin{bmatrix} 0 & 0 & -\dfrac{R_0}{x^{i2}_c + R^2_0}\dot{x}^i_c \end{bmatrix}^{\mathrm{T}} \\ \dot{\boldsymbol{\omega}}_p^{if'_{m-p}} = \begin{bmatrix} 0 & 0 & \dfrac{2R_0 x^i_c \dot{x}^{i\,2}_c}{\left(x^{i2}_c + R^2_0\right)^2} - \dfrac{R_0 \ddot{x}^i_c}{x^{i2}_c + R^2_0} \end{bmatrix}^{\mathrm{T}} \end{cases}. \tag{4}$$

According to the kinematics of the end-effector, fingers move synchronously resulting from the movement of the drive mechanism, and all the opening angles of fingers are equal. Thus, the effector can be regarded as a one degree of freedom (1-DOF) mechanism, although all three fingers can move and can be described through x^i_c of the driving mechanism. In addition, the state of the end-effector changes within a certain range since the motion of the driving mechanism is restricted.

In this study, the driving wheel is 0.8 kg, R_0=0.2 m, and rotary inertia matrix $\boldsymbol{I}_{R_0}$ expressed in f^i_h is diag([0.017; 0.017; 0.033]) kg·m^2. Each finger of the end-effector is 2.5 kg and 0.5 m long, and the rotary inertia matrix $\boldsymbol{I}_{\text{fin}}$ expressed in $f^i_{\text{fin}\_p}$ is diag([7.65e-4; 0.208; 0.208]) kg·m^2. The two extreme states of the effector are shown in Fig. 6(a)−Fig. 6(b), the positions of the end tip projected in a plane are shown in Fig. 6(c).

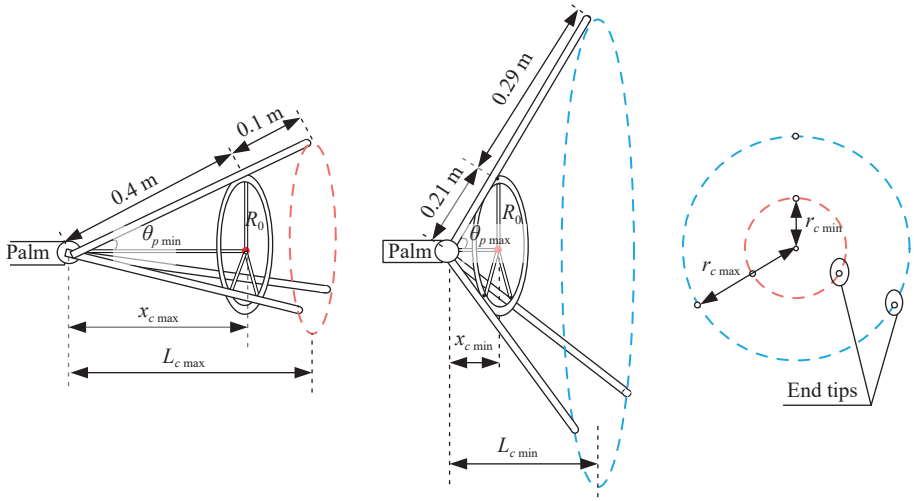

(a) Closed state (b) Opened state (c) Projected view

Fig. 6 Two extreme states of the effector

The deformation range of the end-effector is listed in Table 1.

Table 1 Deformation range of the end-effector

Parameter	Range	
	Closed	Opened
x_c/m	0.350	0.050
θ_p/(°)	30.000	75.964
L_c/m	0.433	0.121
r_c/m	0.250	0.485

2.3 Dynamic model of the robotic system with the hand-shaped deformable end-effector

When the effector is not modeled together with the arm, the operation design and the control of the effectors are usually independent of the arm. This may hide some of the overall capabilities and characteristics of the robot system, which influences the operation design and effect. Therefore, the proposed deformable end-effector is modeled together with the arm as a complete robotic system here.

The imaginary scene of the dual-arm robot and the target is shown in Fig. 7. The coordinate system of the robot body is defined as f_b and the coordinate system of the jth link is defined as f_j. Each robotic arm consists of four conventional links and a deformable end-effector. The joint linked to the end-effector is combined with three short and mutually perpendicular revolute joints and is simplified as a spherical hinge with 3-DOF when modeling. All other joints are column hinges with 1-DOF. Combined with a 1-DOF deformable end-effector, each arm owns 8-DOFs.

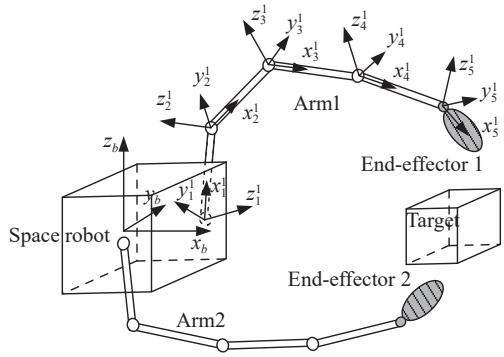

Fig. 7 Imaginary scene of the robot and its operation target

Based on [28,29], the velocity of the robot in each DOF is selected as the generalized velocity. For the robot body, generalized velocities are displacement velocity ($\dot{\boldsymbol{R}} \in \mathbf{R}^{3\times1}$) and angular velocity ($\boldsymbol{\omega} \in \mathbf{R}^{3\times1}$); for the arm, they are the angular velocities of each joint ($\boldsymbol{\omega}_j^i \in \mathbf{R}^{7\times1}$). Here, the deformable end-effector owns 1-DOF, so the whole robotic system owns 22-DOFs, and its generalized velocity matrix is defined as

$$\begin{cases} \dot{\boldsymbol{X}}_b = \begin{bmatrix} \dot{\boldsymbol{R}}^{\mathrm{T}} & \boldsymbol{\omega}^{\mathrm{T}} \end{bmatrix}^{\mathrm{T}} \\ \dot{\boldsymbol{X}}_{a1} = \begin{bmatrix} \boldsymbol{\omega}_1^{1\mathrm{T}} & \boldsymbol{\omega}_2^{1\mathrm{T}} & \cdots & \boldsymbol{\omega}_5^{1\mathrm{T}} & \dot{x}_c^1 \end{bmatrix}^{\mathrm{T}} \\ \dot{\boldsymbol{X}}_{a2} = \begin{bmatrix} \boldsymbol{\omega}_1^{2\mathrm{T}} & \boldsymbol{\omega}_2^{2\mathrm{T}} & \cdots & \boldsymbol{\omega}_5^{2\mathrm{T}} & \dot{x}_c^2 \end{bmatrix}^{\mathrm{T}} \\ \dot{\boldsymbol{X}} = \begin{bmatrix} \dot{\boldsymbol{X}}_b^{\mathrm{T}} & \dot{\boldsymbol{X}}_{a1}^{\mathrm{T}} & \dot{\boldsymbol{X}}_{a2}^{\mathrm{T}} \end{bmatrix}^{\mathrm{T}} \end{cases}. \tag{5}$$

The dynamic equation of the system [30] can be written in the following compact form:

$$\boldsymbol{M}\ddot{\boldsymbol{X}} = \boldsymbol{Q} - \boldsymbol{F}_{\mathrm{nonlinear}} \tag{6}$$

where $\boldsymbol{M} \in \mathbf{R}^{22\times22}$ represents the symmetric mass matrix of the system:

$$\boldsymbol{M} = \begin{bmatrix} \boldsymbol{M}_b & \boldsymbol{M}^1_{\mathrm{cpl\_arm}} & \boldsymbol{M}^1_{\mathrm{cpl\_hand}} & \boldsymbol{M}^2_{\mathrm{cpl\_arm}} & \boldsymbol{M}^2_{\mathrm{cpl\_hand}} \\ \boldsymbol{M}^{1\ \mathrm{T}}_{\mathrm{cpl\_arm}} & \boldsymbol{M}^1_{\mathrm{arm}} & \boldsymbol{M}^1_{\mathrm{hand}} & \mathbf{0}_{7\times7} & \mathbf{0}_{7\times7} \\ \boldsymbol{M}^{1\ \mathrm{T}}_{\mathrm{cpl\_hand}} & \boldsymbol{M}^{1\ \mathrm{T}}_{\mathrm{hand}} & \boldsymbol{I}^1_{\mathrm{hand}} & \mathbf{0}_{1\times7} & \mathbf{0} \\ \boldsymbol{M}^{2\ \mathrm{T}}_{\mathrm{cpl\_arm}} & \mathbf{0}_{7\times7} & \mathbf{0}_{7\times1} & \boldsymbol{M}^2_{\mathrm{arm}} & \boldsymbol{M}^2_{\mathrm{hand}} \\ \boldsymbol{M}^{2\ \mathrm{T}}_{\mathrm{cpl\_hand}} & \mathbf{0}_{7\times7} & \mathbf{0} & \boldsymbol{M}^{2\ \mathrm{T}}_{\mathrm{hand}} & \boldsymbol{I}^2_{\mathrm{hand}} \end{bmatrix} \tag{7}$$

where $\boldsymbol{M}_{\mathrm{b}}$ reflects the dynamic characteristics of the robot body. $\boldsymbol{M}^i_{\mathrm{cpl\_arm}}$ suggests the dynamic coupling between the ith arm and the body. $\boldsymbol{M}^i_{\mathrm{arm}}$ reflects the dynamic characteristics of the ith arm. In addition to the inherent physical properties, they are also related to the current state of the robot and are time-varying. $\boldsymbol{M}^i_{\mathrm{cpl\_hand}}$ represents the coupling between the ith end-effector and the body. $\boldsymbol{M}^i_{\mathrm{hand}}$ and $\boldsymbol{I}^i_{\mathrm{hand}}$ reflect the dynamic characteristics of the ith effector. These variables are calculated according to the mass, static moments, inertia moments, the structure and state of each satellite component.

On the right side of (6), $\boldsymbol{Q} \in \mathbf{R}^{22\times1}$ represents the forces and torques acting on the robot, such as the contact forces. $\boldsymbol{F}_{\mathrm{nonlinear}} \in \mathbf{R}^{22\times1}$ reflects the nonlinear coupling terms of the robot whose amplitude is directly proportional to the intensity of robot motion.

There are some assumptions of the robotic system in the mathematical model:

(i) All the joints of the robotic system are ideal;

(ii) The motors of the driving mechanism are not considered when modeling.

2.4 Motion adjustment using deformable end-effector

The movement of the end tips along its axis of symmetry is one of the most likely motion adjustments of the robotic system during contact since it changes the contact strength in the most efficient direction. In this subsection, this movement is generated through the deforma-

tion of the end-effectors and the robotic arms respectively. Benefiting from the deformation ability of the end-effector, the movement can easily be obtained through the configuration changing of the end-effector itself rather than the adjustment of all joints.

As is shown in Fig. 8. the end tips are expected to retreat by 0.2 m along their axis of symmetry, and the task is carried out respectively by the deformation of the end-effector and the motion of the arm joints. The physical parameters of the robot arm are listed in Table 2.

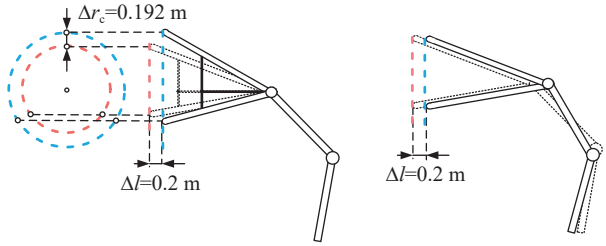

(a) Deformation of the end-effector (b) Motion of all the joints

Fig. 8 End tip motion carried out in two ways

Table 2 Parameters of the robotic arm links

Item	Linear density/(kg/m)	Length/m	$\boldsymbol{S}_j$/(kg·m^2)	$\boldsymbol{I}_j$/(kg·m^2)
Value	5	l_1=0.8	$\boldsymbol{S}_1$=[1.6;0;0]	$\boldsymbol{I}_1$=diag([0.001 2 0.853 0.853])
		l_2=2.5	$\boldsymbol{S}_2$=[15.625;0;0]	$\boldsymbol{I}_2$=diag([0.003 8 26.042 26.042])
		l_3=2	$\boldsymbol{S}_3$=[10;0;0]	$\boldsymbol{I}_3$=diag([0.003 1 13.33 13.33])
		l_4=1	$\boldsymbol{S}_4$=[2.5;0;0]	$\boldsymbol{I}_4$=diag([0.001 5 1.667 1.667])

The task requirements of the effector and the arm joints are listed in Table 3. The largest change among the joint angles is less than 2°, which requires a much higher control precision to guarantee the accuracy of the joint motion response. However, the deformation $\Delta x_c = -0.24$ m of the end-effector is much easier to achieve through rectilinear motion. In addition to the improvement of the motion precision, the deformable effectors greatly simplify the control requirements and reduce the disturbances acting on the robotic system generated from the adjustment of the end tips since the arm joints are avoided from the motion.

Table 3 Deformation task requirement of the effector and the arm joints

Item	Value
Initial position of the geometric center of the end tips/m	[6 1.5 0]
Final position of the geometric center of the end tips/m	[6 1.7 0]
Initial joints configuration/(°)	[16.95 2.28 −37.15 −12.24 −5.07 8.18 −64.26]
Initial x_c/m	0.346 4 (θ_{p0} = 30.29 °)
Demand deformation of x_c/m	−0.241 (Δr_c =0.192 m)
Demand deformation of joints/(°)	[1.9 −0.02 0.06 0.07 −0.27 −0.32 −1.93]

3. Control requirement analysis and high-performance controller design

As is described in Section 2, contact detumbling toward a cubic target with nutation requires a complex operation process. To satisfy the requirements of detumbling, the impedance control method is employed as the theoretical basis for constraining the contact forces. Then, for improving the controller robustness, the error transformation is redesigned. A PPASMC is proposed and employed for the robotic system to achieve the required performances during the operation.

3.1 Impedance control strategy and the controller requirements

For contact detumbling, to avoid consuming too much time caused by weak contact and not to damage the robotic system caused by strong contact, an impedance control strategy [31] is adopted to restrict the contact strength by adjusting the position of the end-effector along the rotating axis of the target. For a certain detumbling process, the contact strength can be estimated from the target motion, target structure and operating capability of the robotic system.

The required adjustment is calculated based on the virtual compliance model of the effector. The mass M_e, damping C_e, and spring K_e of the compliance model are designed based on the real parameters of the effector and the required compliance characteristics. For the ith end-effector, the value of the total force perpendicular to the contact surface is defined as F_p^i. It directly reflects the strength of the contact. Assuming that the difference between the real-time contact force F_p^i and its ideal value F_{pr}^i is ΔF^i

$$\Delta F^i = F^i_{pr} - F^i_p. \tag{8}$$

The expected position movement of the end-effector Δx^i and its time derivative can be calculated reffering to [32] as follows:

$$M_e \Delta \ddot{x}^i + C_e \Delta \dot{x}^i + K_e \Delta x^i = \Delta F^i. \tag{9}$$

Based on the above description, the loop of the detumbling system is shown in Fig. 9. The trajectory planning module includes an open-loop arm approaching before the contact and the closed-loop end-effector movement during the contact. Then, the robotic system contacts the target under control and generates detumbling with the designed contact strength.

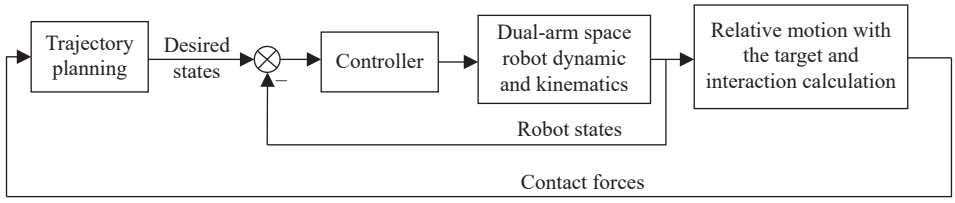

Fig. 9 Loop of the detumbling system

Obviously, to generate the desired detumbling, the robotic system, especially the end-effectors, needs a fast reaction speed and high operation accuracy to withstand the disturbance. At the same time, the coupling characteristics of the designed robotic system installed with the deformable end-effectors make it more difficult to obtain great control performance. Thus, a kind of controller with prescribed performance is suitable for the detumbling operation. In addition, the controller ought to adapt to the unknown inertia parameters of the controlled system and be robust to disturbances during operation.

3.2 Improvement of the error transformation based on prescribed performance

PPC can explicitly define the performances, including the overshoot boundary of the tracking error and its convergence rate through designing the controller parameters. However, in the controller, the existing error boundary is strict on the convergence rate at the beginning and is more useful for rest-to-rest motion. For contact detumbling, the disturbance upon the robotic system is continuous, and the robustness and residual tracking error are more important. Therefore, the boundary of the tracking error is redesigned to improve the performance of the controller.

In a PPC, the tracking error constrained by the boundary is transformed into an unconstrained error through a time-varying function called α. The transformation makes the system more sensitive to the error. Then, the effective controller utilizing the transformed error ensures the performance of the original tracking error.

The value of the original tracking error is defined as $e = x_r - x$, where x_r is the expected generalized state and x is the real state. α is a time-varying monotonically decreasing function, and the value is always positive. Constants δ_L and δ_U represent the scaling factor of the lower and upper overshoot boundaries. The tracking error e satisfies:

$$-\delta_L \alpha < e < \delta_U \alpha. \tag{10}$$

Define $h = e/\alpha$, it yields $h \in (\delta_L, \delta_U)$. Then, a smooth and strictly increasing mapping function [24] is proposed

$$\vartheta_{(t)} = \psi_{(h)} = \frac{1}{2} \ln\left(\frac{\delta_L + h}{\delta_U - h}\right) \tag{11}$$

where $\psi_{(h)}$ takes h as the argument, $\vartheta_{(t)} \in \mathbf{R}$ represents the performance tracking error.

Property 1 $\psi_{(h)}$ inherits the definition domain of the original function and extends the initial value domain to $\mathbf{R}$: $\lim\limits_{h \to -\delta_L} \psi_{(h)} = -\infty$, $\lim\limits_{h \to \delta_U} \psi_{(h)} = \infty$.

The error transformation process is shown in Fig. 10.

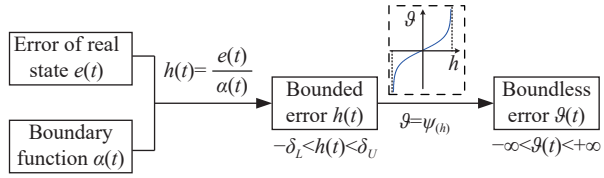

Fig. 10 Error transformation diagram

The transformation function determines that once the original tracking error exceeds the boundary, the transformation process will fail. The characteristic of the boundary function α determines the effect of the error transformation. A commonly used boundary function [24] is as follows:

$$\alpha_{(t)} = (\alpha_0 - \alpha_\infty) \mathrm{e}^{-lt} + \alpha_\infty \tag{12}$$

where the parameters α_0, α_∞, and l are constants of the overshoot boundary and convergence rate that satisfy $\alpha_0 > \alpha_\infty > 0$, $l > 0$; e is the base of the natural logarithm.

Parameter adjustment of the controller is necessary to obtain willing performance. As shown in Fig. 11, for traditional controllers, the adjustment of the controller per-

formance through changing the parameters needs iteration and is experience-dependent. However, according to the time-varying boundary α, the performances of the error are directly defined without iteration and tests.

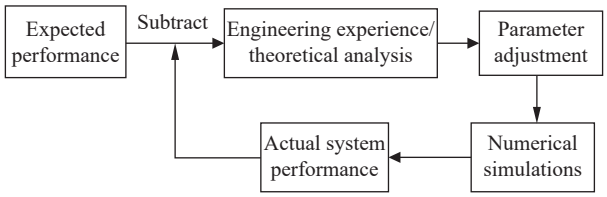

Fig. 11 Design process of the controller parameters

For a strong coupling system such as a space robotic arm, the motion and operation may involve continuous disturbances and may overstep the boundary, as shown in the enlarged figure in Fig. 12.

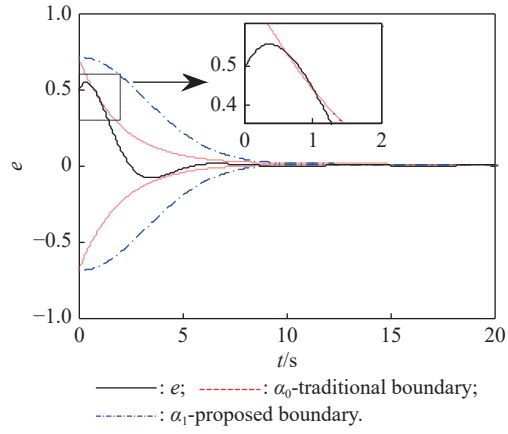

Fig. 12 Time-varying boundary

This risks the effectiveness of the controller. Therefore, a new boundary function is proposed here in which the exponential term is quadratically correlated with time:

$$\alpha_{(t)} = p_1 \mathrm{e}^{-p_2(t-p_3)^2} + p_4 \tag{13}$$

where p_1, p_2, p_3, and p_4 are all positive const that influent the boundary performance.

In Fig. 12, the expressions of the traditional boundary are $\alpha_0=0.7\mathrm{e}^{-0.5t}+0.01$, and the proposed boundary is $\alpha_1=0.7\mathrm{e}^{-0.05(t-0.1)^2}+0.01$. The boundary proposed here liberalizes the restrictions of the system initial values and improves the robustness of the error transformation process.

As shown in Fig. 13, for the determined time, the tracking error after the transformation has the same sign as the error before conversion, and $\vartheta_{e_1} > \vartheta_{e_2}$ when $e_1 > e_2$. In addition, the proportion of the error transformation increases with time. This requires great controller frequency and actuator bandwidth. Additionally, the system is sensitive to the input signal. When the system suffers from disturbances, the controller is weak to deal with the disturbances.

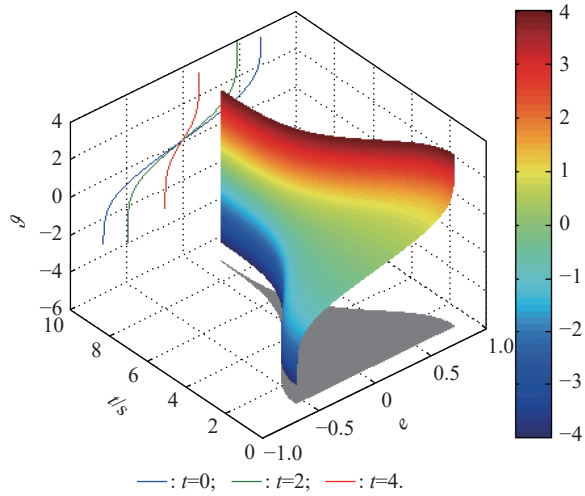

Fig. 13 Characters of transformation error

3.3 Design of the adaptive sliding mode controller with prescribed performance

Aiming to obtain robustness and rapidity of the response of the sliding mode controller and to adapt to the unknown system parameters, a distributed adaptive sliding mode controller with prescribed performance for robotic arms and end-effectors is designed in this section.

Referring to (6), to decouple the controller and reduce the number of estimated parameters of the 8-DOF manipulator combined with a deformable end-effector, the principal elements of the mass matrix $\boldsymbol{M}^i_{\text{manip}} = \begin{bmatrix} \boldsymbol{M}^i_{\text{arm}} & \boldsymbol{M}^i_{\text{hand}} \\ \boldsymbol{M}^i_{\text{hand}} & \boldsymbol{I}^i_{\text{hand}} \end{bmatrix} \in \mathbf{R}^{8\times 8}$ are defined as $\boldsymbol{\beta}^i_{\text{manip}} \in \mathbf{R}^{8\times 1}$. The dynamic model of the manipulator can be written as follows:

$$\operatorname{diag}(\boldsymbol{\beta}^i_{\text{manip}})\ddot{\boldsymbol{X}}^i_{\text{manip}} = \boldsymbol{Q}^i_{\text{manip}} + \boldsymbol{f}^i_{\text{manip}} \tag{14}$$

where $\boldsymbol{f}^i_{\text{manip}}$ represents the sum of nonlinear parts and the elements at nonprincipal element positions in matrix $\boldsymbol{M}^i_{\text{manip}}$.

Contact detumbling is an accurate operation that requires the manipulator to be steady. When the motion of the manipulators is slight and gentle, the system parameters can be regarded as constant through the frozen-coefficient theory. The $\boldsymbol{\beta}^i_{\text{manip}}$ and $\boldsymbol{f}^i_{\text{manip}}$ in (14) can be regarded as the const $\bar{\boldsymbol{\beta}}^i_{\text{manip}}$ and $\bar{\boldsymbol{f}}^i_{\text{manip}}$. Equation (14) can be rewritten as

$$\operatorname{diag}(\bar{\boldsymbol{\beta}}^i_{\text{manip}})\ddot{\boldsymbol{X}}^i_{\text{manip}} = \boldsymbol{Q}^i_{\text{manip}} + \bar{\boldsymbol{f}}^i_{\text{manip}}. \tag{15}$$

Set the expected value of the second-order generalized state to zero, then

$$\ddot{\boldsymbol{e}}^i_{\text{manip}} = -\text{diag}(\bar{\boldsymbol{\beta}}^i_{\text{manip}})^{-1}\left(\boldsymbol{Q}^i_{\text{manip}} + \bar{\boldsymbol{f}}^i_{\text{manip}}\right). \tag{16}$$

According to the definition of the transformed error ϑ, for each signal, the first time derivative of the performance error is

$$\dot{\vartheta} = \frac{\mathrm{d}\vartheta}{\mathrm{d}h}\cdot\frac{\mathrm{d}h}{\mathrm{d}t} = \frac{\mathrm{d}\vartheta}{\mathrm{d}h}\left(\frac{\partial h}{\partial e}\dot{e} + \frac{\partial h}{\partial \alpha}\dot{\alpha}\right). \tag{17}$$

Since

$$\begin{cases} \dfrac{\mathrm{d}\vartheta}{\mathrm{d}h} = \dfrac{1}{2}\left(\dfrac{1}{\delta_L + h} + \dfrac{1}{\delta_U - h}\right) \\ \dfrac{\partial h}{\partial e} = \dfrac{1}{\alpha} \\ \dfrac{\partial h}{\partial \alpha} = -\dfrac{e}{\alpha^2} \end{cases},$$

then

$$\dot{\vartheta} = \frac{1}{2}\left(\frac{1}{\delta_L + h} + \frac{1}{\delta_U - h}\right)\left(\frac{\dot{e}}{\alpha} - \frac{e}{\alpha^2}\dot{\alpha}\right). \tag{18}$$

Based on (17), the second derivative of ϑ is sorted as

$$\ddot{\vartheta} = C\ddot{e} + D \tag{19}$$

where

$$\begin{cases} C = \dfrac{\mathrm{d}\vartheta}{\mathrm{d}h}\cdot\dfrac{\partial h}{\partial e} = \dfrac{1}{2\alpha}\left(\dfrac{1}{\delta_L + h} + \dfrac{1}{\delta_U - h}\right) \\ D = \dfrac{\mathrm{d}^2\vartheta}{\mathrm{d}h^2}\left(\dfrac{\mathrm{d}h}{\mathrm{d}t}\right)^2 + \dfrac{\mathrm{d}\vartheta}{\mathrm{d}h}\left(\dfrac{\partial^2 h}{\partial e\,\partial t}\dot{e} + \dfrac{\partial^2 h}{\partial \alpha\,\partial t}\dot{\alpha} + \dfrac{\partial h}{\partial \alpha}\ddot{\alpha}\right) = \\ \quad \dfrac{1}{2}\left(\dfrac{1}{(\delta_U - h)^2} - \dfrac{1}{(\delta_L + h)^2}\right)\left(\dfrac{\dot{e}}{\alpha} - \dfrac{e}{\alpha^2}\dot{\alpha}\right)^2 + \\ \quad \dfrac{1}{2}\left(\dfrac{1}{\delta_L + h} + \dfrac{1}{\delta_U - h}\right)\left(\dfrac{-2\alpha\dot{\alpha}\dot{e} + 2\dot{\alpha}^2 e - \alpha\ddot{\alpha}e}{\alpha^3}\right) \end{cases}.$$

Written as a vector, the $\ddot{\boldsymbol{\vartheta}}^i_{\text{manip}} \in \mathbf{R}^{8\times 1}$ of an 8-DOF manipulator is

$$\ddot{\boldsymbol{\vartheta}}^i_{\text{manip}} = \text{diag}(\boldsymbol{C}^i_{\text{manip}})\ddot{\boldsymbol{e}}^i_{\text{manip}} + \boldsymbol{D}^i_{\text{manip}} \tag{20}$$

where $\boldsymbol{C}^i_{\text{manip}} \in \mathbf{R}^{8\times 1}$ and $\boldsymbol{D}^i_{\text{manip}} \in \mathbf{R}^{8\times 1}$ are the combination of the C and D of each DOF.

The sliding surface of the controller is defined as

$$\boldsymbol{s}^i_{\text{manip}} = \lambda\boldsymbol{\vartheta}^i_{\text{manip}} + \dot{\boldsymbol{\vartheta}}^i_{\text{manip}}. \tag{21}$$

Substituted by (16) and (20), the time derivative of (21) can be written as

$$\dot{\boldsymbol{s}}^i_{\text{manip}} = \lambda\ddot{\boldsymbol{\vartheta}}^i_{\text{manip}} + \boldsymbol{D}^i_{\text{manip}} - \text{diag}\left(\frac{\boldsymbol{C}^i_{\text{manip}}}{\bar{\boldsymbol{\beta}}^i_{\text{manip}}}\right)\left(\boldsymbol{Q}^i_{\text{manip}} + \bar{\boldsymbol{f}}^i_{\text{manip}}\right). \tag{22}$$

The sliding mode controller consists of two parts:

$$\boldsymbol{Q}^i_{\text{manip}} = \boldsymbol{Q}^i_{\text{eq}} + \boldsymbol{Q}^i_{\text{un}}. \tag{23}$$

The $\boldsymbol{Q}^i_{\text{eq}}$ is derivated to obtain $\dot{\boldsymbol{s}}^i_{\text{manip}} = \boldsymbol{0}$ in (22):

$$\boldsymbol{Q}^i_{\text{eq}} = \text{diag}\left(\frac{\bar{\boldsymbol{\beta}}^i_{\text{manip}}}{\boldsymbol{C}^i_{\text{manip}}}\right)\left(\lambda\dot{\boldsymbol{\vartheta}}^i_{\text{manip}} + \boldsymbol{D}^i_{\text{manip}}\right) - \bar{\boldsymbol{f}}^i_{\text{manip}}. \tag{24}$$

Let $\hat{\boldsymbol{\beta}}^i_{\text{manip}}$ and $\hat{\boldsymbol{f}}^i_{\text{manip}}$ represent the estimations of $\bar{\boldsymbol{\beta}}^i_{\text{manip}}$ and $\bar{\boldsymbol{f}}^i_{\text{manip}}$. The errors between the real parameters and estimated ones are:

$$\begin{cases} \boldsymbol{e}^i_{\beta} = \hat{\boldsymbol{\beta}}^i_{\text{manip}} - \bar{\boldsymbol{\beta}}^i_{\text{manip}} \\ \boldsymbol{e}^i_{f} = \hat{\boldsymbol{f}}^i_{\text{manip}} - \bar{\boldsymbol{f}}^i_{\text{manip}} \end{cases}. \tag{25}$$

Equation (24) can be rewritten as

$$\boldsymbol{Q}^i_{\text{eq}} = \text{diag}\left(\frac{\hat{\boldsymbol{\beta}}^i_{\text{manip}}}{\boldsymbol{C}^i_{\text{manip}}}\right)\left(\lambda\dot{\boldsymbol{\vartheta}}^i_{\text{manip}} + \boldsymbol{D}^i_{\text{manip}}\right) - \hat{\boldsymbol{f}}^i_{\text{manip}}. \tag{26}$$

According to the theory of the exponential approach law, $\boldsymbol{Q}^i_{\text{un}}$ guarantees that

$$\dot{\boldsymbol{s}}^i_{\text{manip}} = -k\boldsymbol{s}^i_{\text{manip}} - \varepsilon\cdot\text{sgn}(\boldsymbol{s}^i_{\text{manip}}). \tag{27}$$

So

$$\boldsymbol{Q}^i_{\text{un}} = \text{diag}\left(\frac{\hat{\boldsymbol{\beta}}^i_{\text{manip}}}{\boldsymbol{C}^i_{\text{manip}}}\right)\cdot\left(k\cdot\boldsymbol{s}^i_{\text{manip}} + \varepsilon\cdot\text{sgn}(\boldsymbol{s}^i_{\text{manip}})\right). \tag{28}$$

According to the definition of $\boldsymbol{C}^i_{\text{manip}}$ in (19), its value increases greatly over time, so it is not suitable to simplify the coefficient in (28) into a constant.

The complete controller is written as

$$\boldsymbol{Q}^i_{\text{manip}} = \text{diag}\left(\frac{\hat{\boldsymbol{\beta}}^i_{\text{manip}}}{\boldsymbol{C}^i_{\text{manip}}}\right)\left(\lambda\dot{\boldsymbol{\vartheta}}^i_{\text{manip}} + \boldsymbol{D}^i_{\text{manip}} + k\boldsymbol{s}^i_{\text{manip}} + \varepsilon\cdot\text{sgn}(\boldsymbol{s}^i_{\text{manip}})\right) - \hat{\boldsymbol{f}}^i_{\text{manip}} \tag{29}$$

where k is a unitless positive constant.

The update laws for estimated parameters of the system are

$$\begin{cases} \dot{\boldsymbol{e}}_{\beta_n} = \boldsymbol{\Gamma}_1\text{diag}(\lambda\dot{\boldsymbol{\vartheta}}^i_{\text{manip}} + \boldsymbol{D}^i_{\text{manip}})\boldsymbol{s} \\ \dot{\boldsymbol{e}}_{f_n} = -\boldsymbol{\Gamma}_2\text{diag}(\boldsymbol{C}^i_{\text{manip}})\boldsymbol{s} \end{cases} \tag{30}$$

where $\boldsymbol{\Gamma}_1, \boldsymbol{\Gamma}_2 \in \mathbf{R}^{8\times 8}$ are unitless constant matrices.

Theorem 1 For the robotic arms described in (14), the controller (29) and the parameter update laws in (30) ensure that the tracking errors of the arms are within the prescribed boundaries and asymptotic tracking is achieved.

Proof Considering the following Lyapunov function:

$$V = \frac{1}{2}\left(\boldsymbol{s}^i_{\text{manip}}\right)^{\mathrm{T}}\text{diag}\left(\hat{\boldsymbol{\beta}}^i_{\text{manip}}\right)\boldsymbol{s}^i_{\text{manip}} + \frac{1}{2}\boldsymbol{e}_{\beta_n}{}^{\mathrm{T}}\boldsymbol{\Gamma}_1^{-1}\boldsymbol{e}_{\beta_n} + \frac{1}{2}\boldsymbol{e}_{f_n}{}^{\mathrm{T}}\boldsymbol{\Gamma}_2^{-1}\boldsymbol{e}_{f_n}, \tag{31}$$

its first derivative is

$$\dot{V} = \boldsymbol{s}^i_{\text{manip}}{}^{\text{T}}\text{diag}\left(\hat{\boldsymbol{\beta}}^i_{\text{manip}}\right)\dot{\boldsymbol{s}}^i_{\text{manip}} + \boldsymbol{e}_{\beta_n}{}^{\text{T}}\boldsymbol{\Gamma}_1^{-1}\dot{\boldsymbol{e}}_{\beta_n} + \boldsymbol{e}_{f_n}{}^{\text{T}}\boldsymbol{\Gamma}_2^{-1}\dot{\boldsymbol{e}}_{f_n}. \tag{32}$$

Define:

$$\begin{cases} \dot{V}_1 = \left(\boldsymbol{s}^i_{\text{manip}}\right)^{\text{T}}\text{diag}\left(\hat{\boldsymbol{\beta}}^i_{\text{manip}}\right)\dot{\boldsymbol{s}}^i_{\text{manip}} \\ \dot{V}_2 = \boldsymbol{e}_{\beta_n}{}^{\text{T}}\boldsymbol{\Gamma}_1^{-1}\dot{\boldsymbol{e}}_{\beta_n} \\ \dot{V}_3 = \boldsymbol{e}_{f_n}{}^{\text{T}}\boldsymbol{\Gamma}_2^{-1}\dot{\boldsymbol{e}}_{f_n} \end{cases}. \tag{33}$$

Rewrite (32) as follows:

$$\dot{V} = \dot{V}_1 + \dot{V}_2 + \dot{V}_3. \tag{34}$$

Substituting (29) into $\dot{V}_1$ leads that

$$\dot{V}_1 = \left(\boldsymbol{s}^i_{\text{manip}}\right)^{\text{T}}\left[-\text{diag}\left(\lambda\dot{\boldsymbol{\vartheta}}^i_{\text{manip}} + \boldsymbol{D}^i_{\text{manip}}\right)\boldsymbol{e}_{\beta_n} + \text{diag}\left(\boldsymbol{C}^i_{\text{manip}}\right)\boldsymbol{e}_{f_n}\right] - \left(\boldsymbol{s}^i_{\text{manip}}\right)^{\text{T}}\text{diag}\left(\hat{\boldsymbol{\beta}}^i_{\text{manip}}\right)\cdot\left(\ k\boldsymbol{s}^i_{\text{manip}} + \varepsilon\cdot\text{sgn}\left(\boldsymbol{s}^i_{\text{manip}}\right)\ \right). \tag{35}$$

Substituting (30) into $\dot{V}_2$ and $\dot{V}_3$ leads that

$$\begin{cases} \dot{V}_2 = \left(\boldsymbol{s}^i_{\text{manip}}\right)^{\text{T}}\text{diag}\left(\lambda\dot{\boldsymbol{\vartheta}}^i_{\text{manip}} + \boldsymbol{D}^i_{\text{manip}}\right)\boldsymbol{e}_{\beta_n} \\ \dot{V}_3 = -\left(\boldsymbol{S}^i_{\text{manip}}\right)^{\text{T}}\text{diag}\left(\boldsymbol{C}^i_{\text{manip}}\right)\boldsymbol{e}_{f_n} \end{cases}. \tag{36}$$

Therefore, it is clear that

$$\dot{V} = -k\cdot\left(\boldsymbol{s}^i_{\text{manip}}\right)^{\text{T}}\text{diag}\left(\hat{\boldsymbol{\beta}}^i_{\text{manip}}\right)\boldsymbol{s}^i_{\text{manip}} - \varepsilon\boldsymbol{s}^i_{\text{manip}}{}^{\text{T}}\text{diag}\left(\hat{\boldsymbol{\beta}}^i_{\text{manip}}\right)\text{sgn}\left(\boldsymbol{s}^i_{\text{manip}}\right). \tag{37}$$

$\hat{\boldsymbol{\beta}}^i_{\text{manip}}$ is the estimation of the principal elements of the arms' mass matrix, which is positive. There are positive k and ε satisfying

$$-k\cdot\left(\boldsymbol{s}^i_{\text{manip}}\right)^{\text{T}}\text{diag}\left(\hat{\boldsymbol{\beta}}^i_{\text{manip}}\right)\boldsymbol{s}^i_{\text{manip}} - \varepsilon\left(\boldsymbol{s}^i_{\text{manip}}\right)^{\text{T}}\text{diag}\left(\hat{\boldsymbol{\beta}}^i_{\text{manip}}\right)\text{sgn}\left(\boldsymbol{s}^i_{\text{manip}}\right) < 0. \tag{38}$$

Consequently, $\dot{V}$ is guaranteed negative definite. According to $\dot{V} = 0$, the invariant set of the system is $\left\{\left(\boldsymbol{s}^i_{\text{manip}}, \dot{\boldsymbol{e}}_{\beta_n}, \dot{\boldsymbol{e}}_{f_n}\right) \mid \boldsymbol{s}^i_{\text{manip}} = \boldsymbol{0},\ \dot{\boldsymbol{e}}_{\beta_n} = \boldsymbol{0},\ \dot{\boldsymbol{e}}_{f_n} = \boldsymbol{0}\right\}$, which indicates that the system is stable under the control shown in (29) and the errors, shown in (25), converge to constant values. □

Hence, the prescribed performance of the tracking errors is satisfied through the proposed controller. According to the above description, the controller structure is shown in Fig. 14.

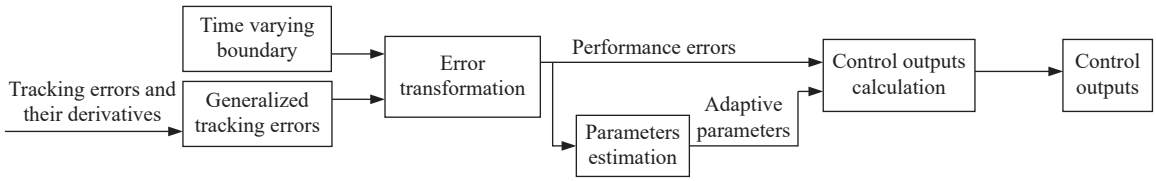

Fig. 14 Controller structure

4. Numerical simulations of the contact detumbling and performance analysis

In this section, MATLAB/Simulink simulations are developed to verify the effect of the contact detumbling operation based on the proposed deformable end-effector and the adaptive sliding mode controller with prescribed performance. The employed robotic arm is described in Table 2. According to the description in Section 2, during contact detumbling, the end tips of the effector are controlled to contact the surface of the target from two sides. At the same time, the deformation of the end-effector and the rotation of the sphere joint linking to the end-effector are designed to steady the contact and restrict the contact strength. The expected contact force of one side is 0.4 N.

The first simulation compares the detumbling with undeformable or deformable end-effectors when using the same sliding mode controller. The parameters of the controller and target are listed in Table 4.

Table 4 Simulation parameters

Item	Value
SMC	$\lambda_{\text{arm}} = \lambda_{\text{claw}} = 3$ $k_{\text{arm}} = k_{\text{claw}} = 120$ $\varepsilon_{\text{arm}} = \varepsilon_{\text{claw}} = 0.01$
PPASMC	$\lambda_{\text{arm}} = \lambda_{\text{claw}} = 3$ $\boldsymbol{\Gamma}_1 = \text{diag}([\ 20\quad 20\quad 20\quad 20\quad 20\quad 20\quad 20\quad 0.05\ ])$ $\boldsymbol{\Gamma}_2 = \text{diag}([\ 3\quad 3\quad 3\quad 3\quad 3\quad 3\quad 3\quad 0.5\ ])$ $\boldsymbol{p}_{\text{arm}} = [\ 0.2\quad 0.5\quad 5\quad 0.1\ ]$ $\boldsymbol{p}_{\text{claw}} = [\ 0.2\quad 0.2\quad 20\quad 0.1\ ]$ $k_{\text{arm}} = 10\quad k_{\text{claw}} = 5$ $\varepsilon_{\text{arm}} = \varepsilon_{\text{claw}} = 0.001$

Continued

Item	Value
Initial state of the target	m_T = 500 kg, V_T= 1×1×1m^3 $\boldsymbol{\omega}_T$ = [1 20 −1]° /s $\boldsymbol{R}_T$ = [6 0 0]m
Initial state of the end-effector	x_c=0.1 m
Desired state of the end-effector	x_c=0.17 m
Impedance parameters of the deformable end-effectors	[10 15 10]

When using undeformable end-effectors, the contact strength is not steady, and it is difficult to maintain long-term periodic contact. Three cycles of contact are figured to show the operation results.

The contact forces of one contact point, shown in Fig. 15, suggest that contact with undeformable end-effectors is short-term and that the contact strength changes quickly.

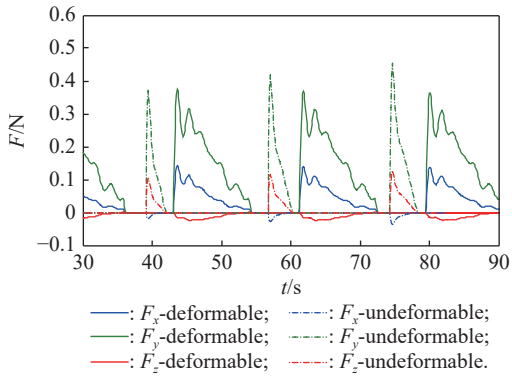

Fig. 15 Contact forces of one contact point

Fig. 16 shows the contact torques and forces to the target resulting from the two end-effectors. The torques generated by the undeformable end-effectors have a higher peak but cannot be maintained. The forces acting on the target may push the target away from the operating space of the robot and are undesired. However, in Fig. 16 (b), the undeformable end-effectors generated more forces and reduced the contact quality.

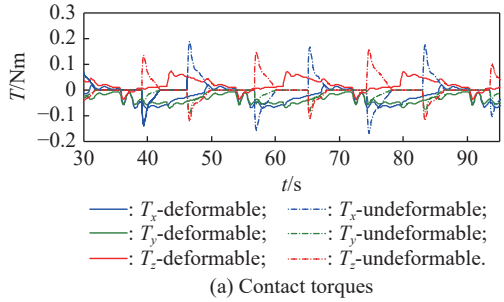

(a) Contact torques

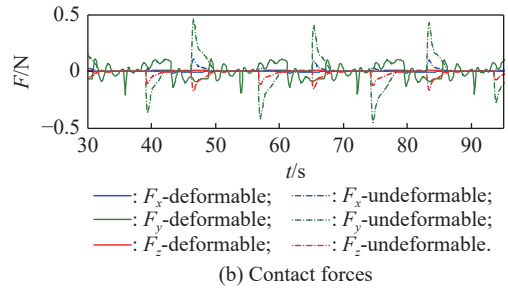

(b) Contact forces

Fig. 16 Contact torques and forces to the target

The above results show that the deformable end-effectors improved contact stability. However, the control performance still needs improvements. Then, the second simulation is generated, which compares the PPASMC and the SMC. The controller parameters are listed in Table 4. To show the details of the controller and robotic system performances, the results of 400−500 s are selected and figured from the 900 s simulation.

Fig. 17 shows the tracking error and the control torques of the sphere joint linked to the end-effector. The required control amplitude is reduced and gentled when using the PPASMC; at the same time, the tracking error of the sphere joint is reduced by approximately two times. The improvement of control performance does not rely on the increase of the controller output amplitude, which reflects the great performance of the PPASMC controller itself.

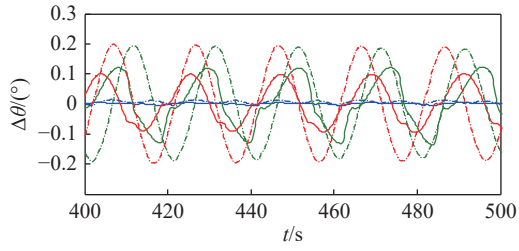

(a) Tracking error of the sphere joint

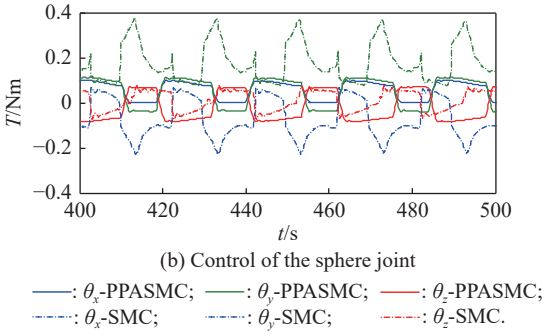

Fig. 17 Control outputs of the sphere joint of arm 1

The tracking error and the control forces of the end-effectors shown in Fig. 18 also reflect that the PPASMC has greater performance. While the control force of the PPASMC is slightly higher than that of the SMC, the peak value of the tracking errors is reduced more than two times when using the PPASMC. The error changes gently when controlled by the PPASMC. Thus, the operation accuracy of the end-effector has been greatly improved.

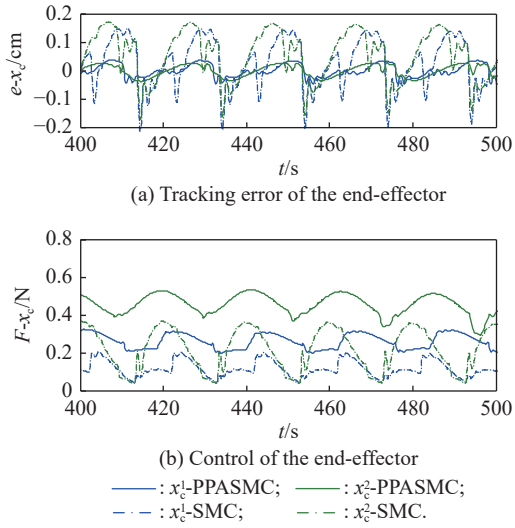

Fig. 18 Tracking error of the end-effectors

The different operation accuracies of the arm and the end-effector lead to different contact states. Fig. 19 shows the distance between the six end tips of the end-effectors and the contact surface. The negative distance means the contact occurred. The distance jumps because of the nutation of the target, and the three tips of one end-effector take turns contacting the target. When controlled by the PPASMC, the end tips jump lower, which means that the state of the relative motion is steadier.

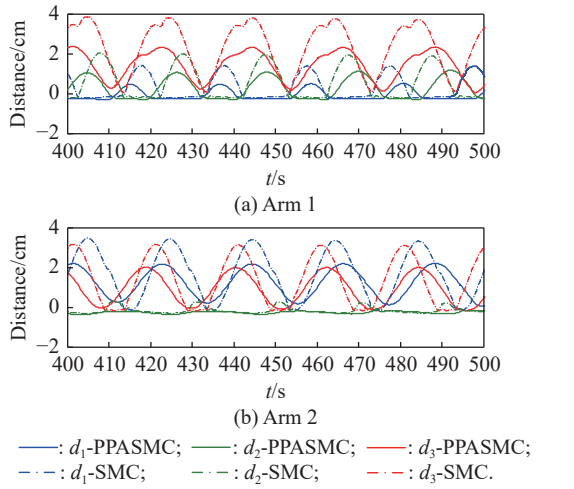

Fig. 19 Distance between the contact points and the target surface

The contact torques generated by one end-effector and the contact forces generated by one of the end tips are shown in Fig. 20. For the contact torque of one end-effector, the results under the PPASMC have a larger amplitude and smoother peak change, which means that the contact state can be maintained for a longer time than that controlled by the SMC. The contact forces of one end tip are compared in Fig. 20(b). When controlled by the PPASMC, the contact forces are approximately two times greater and more steady than those controlled by the SMC.

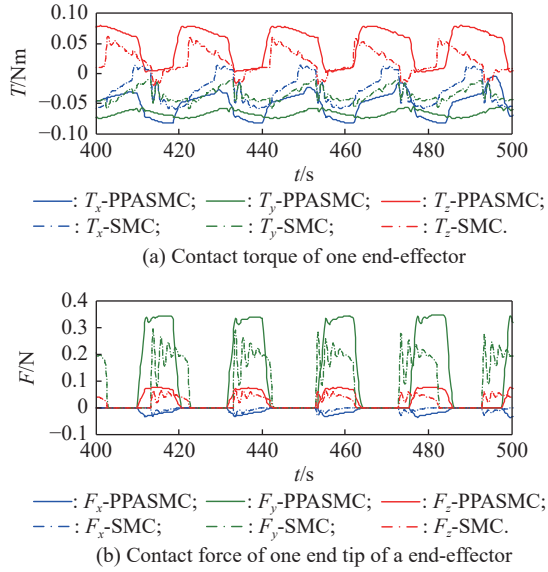

Fig. 20 Contact forces and torques

The different contact states lead to different contact detumbling effects. From the whole 900 s simulation, Fig. 21 shows the angular velocity of the target in three directions. When utilizing the PPASMC, the contact strength is increased, and the angular velocity along the *y*-axis decreases faster. In addition, the nutation of the target is weakened in both simulations.

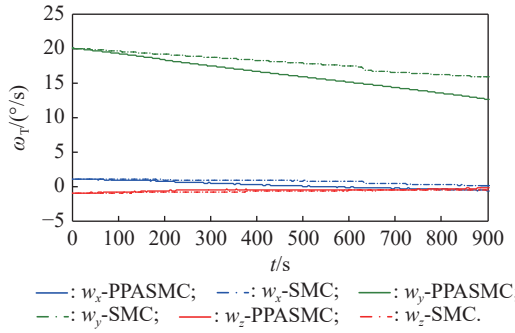

Fig. 21 Angular velocity of the target

The contact forces continuously disturb the robotic system. To overcome the disturbances and maintain the system state, the robot arms are always under control. The control outputs of the first four joints of arm1 are shown in Fig. 22. The control outputs of the PPASMC are significantly smoother than those of the SMC, which is good for the stability of the robotic system.

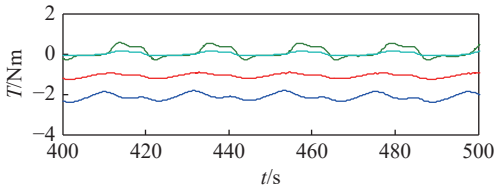

(a) Arm control by PPASMC

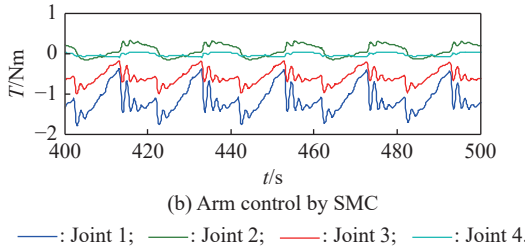

(b) Arm control by SMC

Fig. 22 Control outputs of joint 1−joint 4 of arm 1

In addition to the above simulation figures, some other performances of the 900 s contact detumbling are summarized and listed in Table 5. From the above results, the effectiveness and efficiency of the proposed detumbling method assisted by the deformable end-effector and the PPASMC are verified. The rotation and nutation of the target are reduced simultaneously. When controlled by the PPASMC, even if the amplitude of the control output is not multiplied, the detumbling efficiency increased by nearly 70%. At the same time, the variation range of the target displacement is reduced by approximately 65%, and the variation range of the distance between the end tips and the surface center is reduced by approximately 20%, which shows that the state of the contact detumbling is stabilized by the PPASMC.

Table 5 Simulation results of the approaching

Parameter	Simulation 1	Simulation 2
	PPSMC	SMC
Angular accerleration of target/(°/s^2)	−0.017 7	−0.010 1
Variation range of the target displacement/m	0.008 3	0.024 7
Average value of the normal contact force of one end-effector/N	$\boldsymbol{F}_1=\begin{bmatrix}0.061\\0.350\\0.010\end{bmatrix}$, $\boldsymbol{F}_2=\begin{bmatrix}-0.063\\-0.351\\0.031\end{bmatrix}$	$\boldsymbol{F}_1=\begin{bmatrix}0.027\\0.177\\0.012\end{bmatrix}$, $\boldsymbol{F}_2=\begin{bmatrix}-0.041\\-0.177\\0.029\end{bmatrix}$
Average value of the resultant force and torque acting on the target/(N/Nm)	$\boldsymbol{F}=\begin{bmatrix}5\times10^{-4}\\0\\6\times10^{-4}\end{bmatrix}$, $\boldsymbol{T}=\begin{bmatrix}-0.038\\-0.070\\0.052\end{bmatrix}$	$\boldsymbol{F}=\begin{bmatrix}7\times10^{-4}\\0\\2\times10^{-3}\end{bmatrix}$, $\boldsymbol{T}=\begin{bmatrix}-0.030\\-0.040\\0.025\end{bmatrix}$
Average tracking error of the arm joints/(°)	[0.026 0.022 0.014 0.007 0.003 0.093 0.093]	[0.183 0.038 0.090 0.009 0.006 0.109 0.109]
Variation range of the distance between the end tips and the surface center/m	0.062	0.075

5. Conclusions

Contact detumbling toward a cubic target rotating with nutation is a great challenge and requires the effector and controller of the system to have great performance. According to the motion analysis of the contact area and the contact requirements, a hand-shaped deformable end-effector whose fingers can open and close is designed and modeled to satisfy the detumbling operation. A PPASMC is designed to ensure that the robotic arm and end-effector meet the required tracking error performances and realize impedance contact. Then, the numerical simulations of the contact detumbling using the proposed deformable end-effector and the PPASMC are generated. The simulation results show that contact detumbling is regular and effective when using the proposed effectors and the controller and the contact state is more steady. The angular velocity of the target along all three axes is reduced, which provides a reference for the research of contact detumbling operation toward a cubic nutating target.

References

[1] SHAN M H, GUO J, GILL E. Review and comparison of active space debris capturing and removal methods. Progress in Aerospace Sciences, 2016, 80: 18–32.

[2] SHEN D, LIU J. Analysis of the effectiveness of launch traffic model to the space debris environment. Chinese Journal of Space Science, 2020, 40(3): 349–356. (in Chinese)

[3] HAKIMA H, EMAMI M R. Adaptive detumbling controller for deorbiter cubesat. Proc. of the IEEE Aerospace Conference, 2020. DOI: 10.1109/AERO47225.2020.9172727.

[4] LIU X G, LU Y, ZHANG Q, et al. An application of eddy current effect on the active detumble of uncontrolled satellite with tilt air gap. IEEE Trans. on Magnetics, 2019, 55(12): 1–11.

[5] LI M, ZHANG Y, ZHANG J R, et al. Detumbling method for uncontrolled satellite based on eddy currents. Journal of Guidance, Control, and Dynamics, 2020, 43(8): 1444–1455.

[6] XU W F, YAN L, HU Z H, et al. Area-oriented coordinated trajectory planning of dual-arm space robot for capturing a tumbling target. Chinese Journal of Aeronautics, 2019, 32(9): 2151–2163.

[7] CHEN G, WANG Y Q, WANG Y F, et al. Detumbling strategy based on friction control of dual-arm space robot for capturing tumbling target. Chinese Journal of Aeronautics, 2020, 33(3): 1093–1106.

[8] ZANG Y, ZHANG Y, ZHANG J R, et al. Multipoint contact dynamics and the detumbling strategy for a fast-tumbling target. IEEE Trans. on Aerospace and Electronic Systems, 2019, 56(4): 3113–3122.

[9] LIU Y Q, YU Z W, LIU X F, et al. Active detumbling technology for high dynamic non-cooperative space targets. Multibody System Dynamics, 2019, 47(1): 21–41.

[10] WANG X L, ZHOU Z C, CHEN Y J, et al. Optimal contact control for space debris detumbling and nutation damping. Advances in Space Research, 2020, 66(4): 951–962.

[11] WU S, MOU F L, LIU Q, et al. Contact dynamics and control of a space robot capturing a tumbling object. Acta Astronautica, 2018, 151(10): 532–542.

[12] ONO A, YOKOYAMA K. Laminated-type multi-joint portion drive mechanism and manufacturing method therefor, grasping hand and robot arm provided with the same. The United States: US 2006/0028041 A1, 2006.

[13] HAN F, SUN K, LIU Y, et al. Design, testing and evaluation of an end-effector for self-relocation. Robotica, 2016, 34(12): 2689–2728.

[14] YOSHIDA K, NAKANISHI H. The TAKO (target collaborativize) flyer: a new concept for future satellite servicing. RYCROFT M, CROSBY N, ed. Smaller Satellites: Bigger Business?: 397–399.

[15] PUNNING A, KRUUSMAA M, AABLOO A. Surface resistance experiments with IPMC sensors and actuators. Sensors & Actuators A Physical, 2007, 133(1): 200–209.

[16] FENG F, LIU Y W, LIU H, et al. Design schemes and comparison research of the end-effector of large space manipulator. Chinese Journal of Mechanical Engineering, 2012, 56(4): 674–687.

[17] ZHU M M, XIAO S, YU F. Torque estimation for robotic joint with harmonic drive transmission based on system dynamic characteristics. Journal of Systems Engineering and Electronics, 2022, 33(6): 1320–1331.

[18] GE D M, SUN G H, ZOU Y J, et al. Impedance control of multi-arm space robot for the capture of non-cooperative targets. Journal of Systems Engineering and Electronics, 2020, 31(5): 1051–1061.

[19] WANG X Y, SHI L L, KATUPITIYA J. A strategy to decelerate and capture a spinning object by a dual-arm space robot. Aerospace Science and Technology, 2021, 113: 106682.

[20] LIU X F, ZHANG X Y, CAI G P, et al. A collision control strategy for detumbling a non-cooperative spacecraft by a robotic arm. Multibody System Dynamics, 2021, 53: 225–255.

[21] ZONG L J, LUO J J, WANG M M. Optimal detumbling trajectory generation and coordinated control after space manipulator capturing tumbling targets. Aerospace Science and Technology, 2021, 112: 106626.

[22] BECHLIOULIS C P, ROVITHAKIS G A. Robust adaptive control of feedback linearizable mimo nonlinear systems with prescribed performance. IEEE Trans. on Automatic Control, 2008, 53(9): 2090–2099.

[23] XIA K W, ZOU Y. Neuroadaptive saturated control for relative motion based noncooperative spacecraft proximity with prescribed performance. Acta Astronautica, 2021, 180: 361–369.

[24] YU Z Q, ZHANG Y M, JIANG B. PID-type fault-tolerant prescribed performance control of fixed-wing UAV. Journal of Systems Engineering and Electronics, 2021, 32 (5): 1053−1061.

[25] LIU L X, YAO W, GUO Y. Prescribed performance tracking control of a free-flying flexible-joint space robot with disturbances under input saturation. Journal of the Franklin Institute, 2021, 358(9): 4571–4601.

[26] ZHENG S P, NIU X J, PENG C H. Adaptive super-twisting-tike sliding mode control with prescribed performance for robot manipulators. Journal of Mechanics in Medicine and Biology, 2019, 19(8): 1940053.

[27] WEI C S, LUO J J, DAI H H, et al. Learning-based adaptive prescribed performance control of postcapture space robot-target combination without inertia identifications. Acta Astronautica, 2018, 146: 228–242.

[28] KANE T R, LEVINSON D A. Dynamics: theory and applications. New York: McGraw-Hill, 1985.

[29] TARN T J, SHOULTS G A, YANG S P. A dynamic model of an underwater vehicle with a robotic manipulator using Kane's method. Autonomous Robots, 1996, 3: 269–283.

[30] HU Q, ZHANG J R. Maneuver and vibration control of flexible manipulators using variable-speed control moment gyros. Acta Astronautica, 2015, 113(8/9): 105–119.

[31] HOGAN N. Impedance control: an approach to manipulation. 2. implementation. Proc. of the American Control Conference, 1984: 304−313.

[32] CHOI T Y, CHOI B S, SEO K H. Position and compliance control of a pneumatic muscle actuated manipulator for enhanced safety. IEEE Trans. on Control Systems Technology. 2011, 19(4): 832−842.

Biographies

ZANG Yue was born in 1993. She received her Ph.D. degree in aeronautical and astronautical science and technology from the School of Aerospace Engineering, Beijing Institute of Technology in 2022. Her research interests are spacecraft attitude control and uncontrolled satellite detumbling.
E-mail: zangyue2016@bit.edu.cn.

ZHANG Yao was born in 1985. He received his Ph. D. degree in aeronautical and astronautical science and technology from School of Astronautics, Beihang Unicersity in 2012. He is an associate professor at the School of Aerospace Engineering, Beijing Institute of Technology. His research interests are spacecraft attitude control, spacecraft vibration isolation, spacecraft on-orbit service, and spacecraft cluster dynamics and control.
E-mail: zhangyao@bit.edu.cn.

HU Quan was born in 1987. He received his Ph.D. degree in aeronautical and astronautical science and technology from School of Astronautics, Beihang Unicersity in 2014. He is an associate professor at the School of Aerospace Engineering, Beijing Institute of Technology. His research interests are multibody dynamics, attitude control and vibration suppression of flexible spacecraft, and dynamics and control of space robot.
E-mail: huquan@bit.edu.cn.

LI Mou was born in 1992. He received his Ph. D. degree in aeronautical and astronautical science and technology from the School of Aerospace Engineering, Beijing Institute of Technology in 2021. He is an engineer in China Academy of Space Technology in 2021. His research interests are spacecraft dynamics and control and uncontrolled satellite detumbling.
E-mail: limou2333@163.com.

CHEN Yujun was born in 1981. He received his Ph. D. degree in aeronautical and astronautical science and technology from the School of Aerospace Engineering, Beijing Institute of Technology in 2011. He is is a senior engineer in China Academy of Space Technology. His research interests are spacecraft design and multidisciplinary optimization.
E-mail: chenyj1001@163.com